Renewable Energy 126 (2018) 465–474

Contents lists available at ScienceDirect

Renewable Energy

journal homepage: www.elsevier.com/locate/renene

A new algorithm using a pyramid dataset for calculating shadowing in solar potential mapping

Myeongchan Oh [a], Hyeong-Dong Park [a, b, *]

[a] Department of Energy Systems Engineering, Seoul National University, Seoul 08826, Republic of Korea
[b] Research Institute of Energy and Resources, Seoul National University, Seoul 08826, Republic of Korea

ARTICLE INFO

Article history:
Received 7 September 2017
Received in revised form
20 February 2018
Accepted 26 March 2018
Available online 27 March 2018

Keywords:
Solar potential
GIS
Solar mapping
Shadow calculations
Calculation time
Photovoltaic

ABSTRACT

The efficiency of solar potential mapping is becoming increasingly important as solar energy technologies further develop. As digital surface models (DSMs) with improved spatial resolution become more available, the efficiency and accuracy of calculating solar potential need to be better improved. This study analyzes the algorithms available for calculating shadowing and proposes a new algorithm using a pyramid dataset. The available algorithms can be categorized as either shadow-based calculation algorithm (SBC) or Viewmap-based calculation algorithm (VBC). Relatively, SBC can generate simple results rapidly while VBC can generate detailed results slowly. VBC comprises three algorithm types: line scanning, all-data scanning, and the proposed pyramid dataset algorithms. The calculation time and accuracy of these algorithms were analyzed with respect to the spatial resolution of the DSMs and sky division resolution. The results show that the calculation time for each algorithm increases significantly as the resolution of the DSM increases. The proposed pyramid dataset algorithm showed high calculation speed and time complexity compared to previous VBCs. It is also able to generate a more detailed map than the SBC. The proposed algorithm showed high potential for further study as it can generate a detailed map of high resolution DSM rapidly.

1. Introduction

Solar projects often need to consider spatial distribution as well as irradiance. As solar energy supply increases, solar potential mapping becomes increasingly important. These maps are essential for estimating solar energy capacity from global irradiance to city energy output scale. These maps are used to select sites for power plants and estimate total energy potential, among other purposes.

This study focuses on the city and village scale. At this scale, differences in solar irradiance input are marginal; however, shadowing is important. These small scale solar potential maps become more salient as solar energy systems are installed in complex sites such as urban areas. These areas have many discontinuous structures which cast large shadows. Applying solar potential maps to analyze shadowing is useful in such cases.

Rapid technological development has resulted in increases in data capacity and accuracy. Sensors are typical of this trend. Datasets acquired by sensors with improved spatial and temporal resolutions are common. Similarly, digital surface models (DSMs) or digital elevation models (DEMs) used to map solar potential maps also have improved spatial resolutions. Due to light detection and ranging (LiDAR), stereo image processing algorithms, and unmanned aerial vehicle (UAV) technology, high-resolution DSMs are easily generated with a spatial resolution of less than 1 m, comprising millions of pixels. Areas with high complexity such as urban environments can now be analyzed accurately with these DSMs. However, they have high computation requirements due to the volume of data, which make them more difficult to process. More research is required for efficient data processing methods.

Many literature and studies on solar potential mapping are available. Freitas et al. [1] collated and analyzed existing solar potential modeling tools. For small-scale applications, early models include RADIANCE [2–4], r.sun [5,6], and ArcGIS Solar Analysis [7–12]. RADIANCE models have been applied in later models such as PPF [3,13] and Daysim [14,15]. These models use 3D-modeled data and calculate irradiance by ray tracing methods. Ray tracing is an algorithmic method used in computer graphics to trace light paths to calculate shadowing. These algorithms produce highly

[*] Corresponding author. Department of Energy Systems Engineering, Seoul National University, Seoul 08826, Republic of Korea.
E-mail address: hpark@snu.ac.kr (H.-D. Park).

https://doi.org/10.1016/j.renene.2018.03.068
0960-1481/© 2018 Elsevier Ltd. All rights reserved.

accurate results but also require 3D modeling and high computational power. Ray tracing methods are also used in other models such as SORAM [16].

r.sun and ArcGIS Solar Analysis use raster type data to calculate solar potential. Raster type is a grid based pixel data which is generally compared to vector format. Pixel indicates a unit element in this data type. Raster type have a simple data structure and are easy to generate; however, they allow one height value per pixel and only 2.5D data can be represented. Models using GIS determine shadowing with raster calculations. r.sun and ArcGIS Solar Analysis use slightly different algorithms for calculating shadowing. r.sun was developed for application to large terrains and v.sun [17] was adapted for urban use. ArcGIS Solar Analysis is still widely used as ArcGIS is a well-known software and can be applied to GIS. However, the algorithms used for this model are not efficient and have many restrictions. SOL [18–20] is a recently developed urban-oriented model which uses high-resolution DSM and can calculate the solar potential for building façades. Algorithms for shadowing in these models are explained in Section 2.2.

TOWNSCOPE II [21] and SimStadt [22] are other models that use 3D-modeled data. TOWNSCOPE II is a commercial software used specifically for visualization. It calculates shadowing by considering other 3D-modeled objects. SimStadt uses triangulated 3D surfaces to calculate detailed shadowing. Basic algorithms for calculating shadowing in these models are similar to those used in models using GIS formats. However, the former uses real 3D objects or fractions as calculation units and requires more computational power while the latter uses 2.5 D pixels as calculation units, which produces results rapidly and can be applied to GIS formats. Table 1 shows some of the models described in the literature and their features. The models are grouped into similar algorithm categories.

Many studies analyzed the accuracy of irradiance and solar potential models; yet, few studies have assessed the computational power required to calculate solar potential maps accurately at different resolutions. Ruiz-Arias et al. [23] studied the calculation time and accuracy of four tools but did not analyze the reasons behind the calculation time differences. In addition, as each tool uses different irradiance input data, accuracy analysis is based on not only the algorithm but also the irradiance input.

Calculation efficiency cannot be analyzed without considering the resolutions of the data. If this changes, the calculation time and accuracy also change. Many types of resolution are used including spatial resolution, sky division, and temporal resolutions of weather. Using high-resolution data can result in high accuracy, but this requires long calculation times. For high efficiency, it is important to balance appropriate resolutions with the required accuracy.

2. Methodology

This study mainly focuses on two objectives. The first is to propose a new algorithm to calculate shadowing efficiently with broad application. This algorithm should be able to accurately and rapidly calculate shadowing for DSMs with high spatial resolution. The second is to compare the new algorithm with existing algorithms regarding the calculation time and accuracy. The resolutions of other variables such as sky division resolution are also considered.

Models using raster data are analyzed in this case because they are more accessible and more rapidly processed. Therefore, DSM used in this study is in raster format. Point clouds data can be easily generated by sensors such as LiDAR or UAV. Producing raster data from point clouds is a simple and rapid process. However, producing 3D models, such as mesh types, is more difficult as they require more factors to be resolved.

Algorithms that calculate solar potential differ for each model. Therefore, this study integrates the available models to produce a unified method, except for calculating shadowing. Input irradiance in each case is modified to a “Sunmap” format. Through this unified format and method, all algorithms are analyzed without bias.

2.1. Calculation of solar potential

2.1.1. Sky division

To calculate irradiance and shadowing, previous studies used divisions of sky hemisphere. The various sky division methods with unique advantages include equal-area, equal-angle, and triangles [24]. The International Commission on Illumination (CIE) recommended using 145 equal-area sky divisions; however, other types of sky division also have their own advantages. Equal-area division minimizes spatial distortions, but the index of position of each grid is not easily accessible. Equal-angle division has an advantage in indexing for each grid, but distortions can be generated. To supplement these limitations, this study defines an equal-area-equal-angle division by controlling the zenith angle so that an easily accessible grid with an equal-area can be generated (Fig. 1 (a)). Although this method shows shape differences in each grid, it has the advantages of the equal-area type and equal-angle types. The calculation time for algorithms affected by indexing of sky division can be significantly reduced using this method. For example, part of the Viewmap, which has the same azimuth direction, can be calculated simultaneously in the equal-angle type. However, all

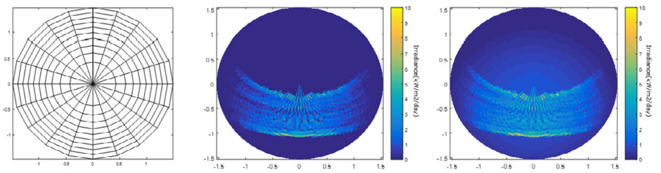

(a) Sky division
(10 ZN, 20 AN)

(b) Sunmap(Beam)
(after AOI calculation)

(c) Make Sunmap(Beam+Diffuse)
(after AOI calculation)

Fig. 1. Examples of (a) Sky division and (b) Sunmap of beam irradiance and (c) Sunmap of total irradiance with a fixed southern 35°.

Table 1
Summary of solar potential calculation models in the literature.

Model name	Geometry format	Algorithm for shadowing calculations	Starting year	References
RADIANCE	3D model	Ray-tracing	1994	[2–4]
r.sun	Raster	Shadow-based calculation	1997	[5,6]
ArcGIS Solar Analysis	Raster	Viewmap-based calculation	1999	[7–12]
PPF	3D model	Ray-tracing	2004	[3,13]
TOWNSCOPE II	3D model	Viewmap-based calculation	2011	[21]
v.sun	3D model	Shadow-based calculation	2012	[17]
Daysim	3D model	Ray-tracing	2013	[14,15]
SimStadt	3D model	Shadow-based calculation	2013	[22]
SORAM	3D model	Ray-tracing	2014	[16]
SOL	Raster	Shadow-based calculation	2014	[18–20]

different azimuth and zenith directions should be calculated when it is not equal-angle type.

Equal-area-equal-angle sky division resolution is defined by the number of azimuth (NA) and the number of zenith (NZ) angles. The azimuth angle is equally divided for each azimuth, whereas the zenith angle is divided by different angles for each zenith. These values are calculated to produce grids of equal area. The generated grid consists of a long zenith length for low zenith angles and a short zenith length for high zenith angles.

2.1.2. Sunmap

Irradiance data, which are solar radiant power per unit area, are processed into the “Sunmap” format. Sunmap comprises irradiance values for each sky division grid; in other words, it represents where irradiance comes from and how much there is. The word Sunmap used in ArcGIS Solar Analysis has a slightly different meaning. In this study, Sunmap includes both beam and diffuse irradiance calculated in each grid in kW/m^2/day. The irradiance intensity and sun position is calculated for each time step and irradiance intensity data are produced for each grid position. The beam irradiance is calculated by adding its value to each corresponding grid. For this study, an isotropic sky diffuse model is assumed for calculating diffuse irradiation. It is the simplest model which can alleviate specificity by region. This model assumes all diffuse irradiance has the same intensity and comes from every direction in the hemisphere. Diffuse horizontal irradiance (DHI) can be calculated for each grid.

$$\text{Isotropic\_diffuse\_irradiance\_per\_grid}_i = \frac{DHI_i \, cos\theta_i}{a\sum_j^z cos\theta_j} \tag{1}$$

In this equation, $\widehat{\theta}$ is zenith angle, a is azimuth number, and z is zenith number.

In this study, Sunmap considers the panel angle for calculating shadowing. Shadowing refers to self-shadowing by the surface of a panel or terrain [25]. To consider the panel angle and calculate irradiance based on the surface, only the normal component of the panel should be considered. All irradiance is multiplied by the cosine of the angle of incidence (AOI) which is the angle between the irradiance and the normal vector of the panel. For fixed solar panel systems, all isotropic diffuse irradiance can be determined simultaneously because the AOI is fixed for each grid.

2.1.3. Shadowing

Shadowing can be calculated from surrounding objects, with many algorithms calculations available. Considering methods used for raster datasets, existing studies can be categorized into two groups. The first is methods based on sun position and shadows. These methods calculate irradiance by simulating solar movement and shadows over time. The results are represented as shadow maps. Many existing studies such as SOL algorithm use a similar approach. The alternate is methods based on Viewmap, which is a map of sky coverage similar to a sky view factor (SVF) that provides information for each shadowed section in the sky division grid. Shadowing can be determined with Viewmap and models such as ArcGIS Solar Analyst use this algorithm. The results are represented as Viewmaps for each pixel. Both methods for calculating shadowing can be combined with Sunmap to produce a solar potential map. A detailed methodology for both approaches is described in Section 2.2.

2.1.4. Solar potential

Solar potential can be expressed in various formats including irradiance and electricity generation. To reduce the number of factors and simplify the process, this study uses irradiance as solar potential which can be calculated from an irradiance input and shadowing analysis. When completing shadow-based calculation (SBC), a simple summation of all shadow maps determines the total irradiance. In this case, each shadow map has a value for irradiance intensity. When completing Viewmap-based calculation (VBC), the irradiance of each pixel is calculated by multiplying the Sunmap and the Viewmap.

2.2. Algorithms for calculating shadowing

2.2.1. Shadow-based calculations

SBC calculates shadows for each sun position. Shadows can be identified using the location and height of all other pixels. The shadows are distinguished by comparing the angle of two pixels and the angle of sun elevation. For each sun position, shadows can be calculated using only one scan of the DSM. The number of required shadow maps is equal to the number of sun positions, which is also equal to the number of grids on the Sunmap. Using a width of DSM (n), height of DSM (m), the NZ (z), and NA (a), the time complexity of shadowing in the SBC is O ($nmza$). As all other processes used to calculate the solar potential have a lower time complexity, the time complexity of calculating shadowing is the total time complexity for this calculation. All processes are shown in Fig. 2 (a).

SBC in r.sun calculate shadows for each pixel separately. In this case, the number of pixels that need scanning is more than the number of pixels in the DSM. Nevertheless, the algorithms used in this study require only one scan because they calculate all the shadows in a line simultaneously. Although these algorithms are slightly different, this study unifies all similar algorithms into the SBC because the results are the same.

2.2.2. Viewmap-based calculation

VBC determines Viewmaps for each pixel. The basic concept of this algorithm was introduced by Fu and Rich [7]. Viewmap represents how much of the sky division grids are shaded by surrounding objects. It can generate position and intensity of solar irradiance in each sky division grid with Sunmap. The words used to describe the sky coverage map was “viewshed” or “Shading mask” in previous studies, but this study uses Viewmap in apposition to Sunmap. Viewmaps are obtained with distances and heights of view point and target points. As raster DSMs do not contain multiple height data, only the highest zenith angle is

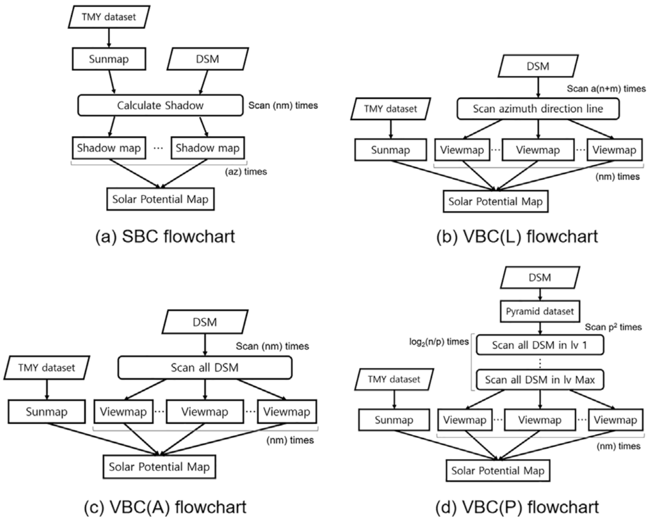

(a) SBC flowchart

(b) VBC(L) flowchart

(c) VBC(A) flowchart

(d) VBC(P) flowchart

Fig. 2. Flowchart of (a) SBC, (b) VBC(L), (c) VBC(A) and (d) VBC(P).

needed for each azimuth angle. Viewmaps need to be created for all pixels to generate a solar potential map and most pixels need to be scanned; thus, VBC requires high computation. Three different algorithms for calculating Viewmaps are analyzed in this study. The first is the algorithm used for existing models, the second is a simple but inefficient algorithm, and the third is the proposed algorithm.

2.2.2.1. Line scanning algorithm. Existing models such as ArcGIS Solar Analysis and TOWNSCOPE II use line-scanning algorithms that use a portion of data from the DSM when calculating Viewmaps. For each position in the DSM, only data in the azimuth direction line are considered. For TOWNSCOPE II, the process is not the same because 3D-modeled data are used. One problem with this algorithm is that data near the view position overlaps and data far from the view point cannot be used. As the number of pixels in the DSM increases, the extent of unused data increases as well. Used pixels in the DSM are shown in Fig. 3 (a) and Fig. 4 (a). Fig. 3 is visualized with a 100 × 100 resolution for the DSM with 60 azimuth divisions.

To calculate Viewmaps in all areas, all processes are iterated the number of times of the pixels in the DSM(nm), and to calculate individual Viewmaps, the data scanning is iterated NA(a) times with the pixel in azimuth line. The average number of pixels used for calculating each azimuth line is $(n + m)/2$. The number of all data points used is $a(n + m)/2$. Thus, calculating Viewmaps in this algorithm has O $(nma(n + m))$ of time complexity (Fig. 2 (b)).

2.2.2.2. All-data scanning algorithm. All-data scanning considers all of the height data in the DSM. This algorithm is simple; however, existing models do not use this algorithm because of its high computational requirements. It calculates the azimuth and zenith angles for all pixels in the DSM and extracts the maximum zenith angle for each azimuth angle. This requires a long computation time and problems are expected to occur with this algorithm. First, there are not enough pixels near the view point to consider all azimuth angles, which means that some objects near the view point may be ignored for specific azimuth angles. Second, the obstruction can be exaggerated as the maximum zenith angle is selected for each azimuth angle. The scanned pixels for this algorithm are shown in Figs. 3 (b) and Fig. 4 (b).

The calculation of zenith and azimuth angles is not time-consuming when using Matlab which can rapidly calculate matrix operations. However, extracting obstructions for each azimuth angle does take time. An extra iteration for this extraction is added to improve performance in Matlab. Although NA(a) was added to the time complexity, the total calculation time was reduced. Theoretically, all-data scanning algorithm needs nm of time complexity; however, the modified code used in this study needs nma of time complexity. Therefore, total time complexity is O (n^2m^2a) (Fig. 2 (c)).

2.2.2.3. Pyramid dataset algorithm. A pyramid dataset comprises multi-scale data which are used for image processing. This new algorithm uses a pyramid format DSM to reduce the calculation time. The principle of this algorithm is to use different spatial resolution data depending on the distance from the view point and to use low resolution data when distance is far. The pyramid dataset comprises the original DSM and subsampled DSMs. The spatial resolution halves for each subsampling. Subsampled DSMs with lower spatial resolutions are at a higher pyramid level (Fig. 5). The number of scanned pixels is significantly reduced when using pyramid datasets, allowing rapid calculation of the Viewmap. Scanned pixels appear similar to those shown in Fig. 3 (b) and (c); however, different pixel sizes can be observed in Fig. 4(b) and (c). Although this algorithm has similar problems to the all-data scanning algorithm, obstruction exaggerations are different because an average height is used.

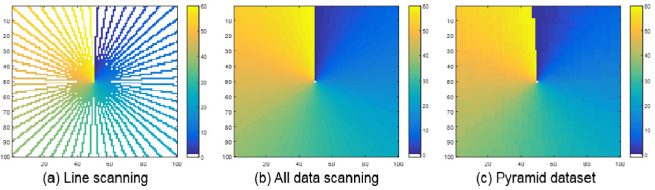
(a) Line scanning (b) All data scanning (c) Pyramid dataset

Fig. 3. Scanned DSM data and their NA. A NA of 0 is not used.

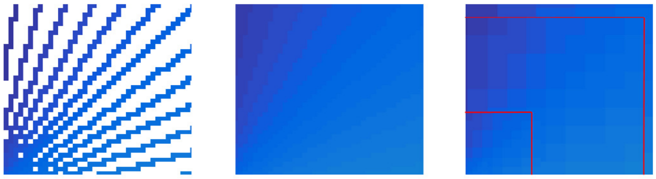
(a) Line scanning (b) All data scanning (c) Pyramid dataset

Fig. 4. Expanded image of Fig. 3 which is scanned DSM data and their NA. The red lines show the border of the pyramid dataset.

The difference between this algorithm and the all-data scanning algorithm is the process of changing the pyramid level. Changes occur in the pyramid level when the distance from the view position is far from the specific value. This value is set as "p" which is the pixel index, with a pixel angle smaller than the azimuth angle of the sky division. If the distance from the view point is larger than p, then the next level of pyramid data is used. Therefore, pixels with a small pixel angle are replaced by pixels at a higher level of the pyramid. The number of pyramid levels required is $log_2(n/p)$ when $n > m$. Thus, the number of data scanned to calculate the Viewmap is expressed as $p^2 {*} log_2(n/p)$. p is a function of a (NA) and a is a tangent function. When a is big enough, p is proportional to a, because the tan(x) function is similar to x when x is close to 0. Therefore, the time complexity of this algorithm is O $(nma^2\log(n/a))$. When n is higher than a, the time complexity is O $(nma^2\log(n))$ (Fig. 2 (d)).

2.3. Comparison of algorithms

Four algorithms — one SBC and three VBCs — were developed and analyzed. The VBCs were divided into three algorithms for calculating shadowing. These VBCs were marked (L) for line scanning, (A) for all-data scanning, and (P) for the pyramid dataset. The comparison of these algorithms is based on calculation time and

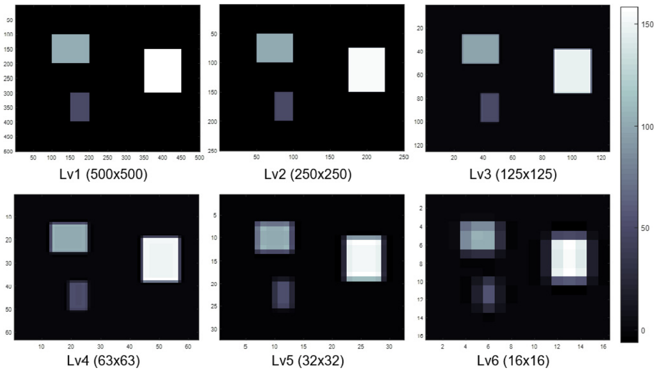
Lv1 (500x500) Lv2 (250x250) Lv3 (125x125)
Lv4 (63x63) Lv5 (32x32) Lv6 (16x16)

Fig. 5. Example of pyramid dataset images. Higher level images have lower spatial resolution which indicates lower number of pixels.

accuracy. The resolution of the DSM and the sky division is considered in the analysis.

This analysis comprises two parts. Firstly, an influence of the spatial resolution of the DSM is analyzed. The resolution of the DSM is set from 100 × 100 to 900 × 900 pixels. Each DSM is of the same form but comprises different pixel sizes. The NZ and NA are constant at 30 and 120, respectively. Secondly, an influence of the sky division resolution is analyzed. The NZ is set from 10 to 60 with an interval of 10, and the NA is set from 20 to 180 with an interval of 20. The resolution of the DSM is set at a constant 500 × 500 pixels.

For each algorithm, the calculation time is measured for each of the processes, from creating a Sunmap to generating a solar potential map. Measuring times are analyzed based on time complexity. To validate the correlation of time complexity and the measured time, a linear trend line is generated with modified x values which are computed to create a linear correlation with the calculation time. As each algorithm has different time complexity, the modified x value also has a different form. The correlation is evaluated by a coefficient of determination, R^2.

Accuracy is analyzed with two error indices: the relative root mean square error (rRMSE) and relative mean bias error (rMBE). The RMSE is the square root of the squared difference and is used to estimate accuracy. A value of 0 indicates 100% accuracy and the higher the value, the lower the accuracy. The rRMSE is a normalized RMSE value, which helps to compare different methods.

$$\mathrm{rRMSE} = \frac{1}{\overline{y}}\sqrt{\frac{\sum_{i=1}^{N}\left(\widehat{y}_i - y_i\right)^2}{N}} \tag{2}$$

$$\mathrm{rMBE} = \frac{\sum_{i=1}^{N}\left(\widehat{y}_i - y_i\right)}{\overline{y}N} \tag{3}$$

In this equation, $\widehat{y}$ is calculated result, y is reference result, $\overline{y}$ is mean value of the reference result, and N is the total number of data in the DSM.

The MBE is the average difference and is used to estimate the bias of the results. A value of 0 means no bias and a positive or negative value indicates a biased result. The relative MBE (rMBE) is also analyzed as index normalized by average reference result. The results of SBC are used as reference results because this algorithm has fewer factors that may produce errors. In the first part, each result of the SBC is used as a reference result. In the second part, the result for the highest NZ and NA determines the reference result.

3. Data

3.1. Input irradiance

Irradiance dataset in this study use the typical meteorological year (TMY) format. A TMY dataset contains virtual hourly data, which are extracted from long-term weather databases. Data used for TMY databases are measured over a 10-year timeframe, indicating long-term features of the target area. The irradiance dataset does not affect the calculation time; however, it can affect the accuracy. This study uses a TMY dataset created by the Korea Institute of Energy Research (KIER). Average expanded uncertainty in this dataset is 3% for GHI and 18% for DNI.

The study area for solar position, latitude, and longitude is set to Seoul, Korea. The TMY dataset is generated in Seoul for measured irradiance. The solar position and intensity is calculated in 12-min steps for one year. The panel angle is set at a fixed southern 35° latitudes. Examples of calculated Sunmaps are shown in Fig. 1 (a) and (b).

3.2. Virtual DSM

A simple virtual DSM (Fig. 6) comprising three square buildings is used to visualize and analyze results. The method can be applied to complex urban areas, but this simple DSM is used to clarify distributional differences generated by discontinuous geometry. In an urban area, many artificial structures produce discontinuous surfaces. For a simple DSM, the differences produced by these discontinuities are easily detected. Also, as only three obstructions exist, errors in Viewmap are easily distinguished. In addition, there is a sufficient amount of flat space between the obstructions to detect the influence of the distant obstructions. As algorithms like VBC(L) remove a lot of data when the distance is far from the view point, using DSMs with obstructions far from the view point can be effective. It also reduces the differences in spatial resolution. In a complex DSM, reducing resolution by resampling produces further errors. The DSM used in this study can be reproduced for all spatial resolutions.

3.3. Processing environment

Matlab is used to determine the solar potential maps. As Matlab shows high performance for matrix operations, making algorithms with matrix operations reduces calculation times. Multithreaded calculations, such as parfor function, are also used with Matlab. GPU operations are not used because algorithms for this study show low performance with GPU operations. Data transfer to GPU is more time-consuming than conducting CPU calculations. All processes were executed with an Intel(R) Core™ i5-4690 CPU @ 3.50 GHz (4 CPUs) workstation with 16 GB of RAM.

4. Results

4.1. Calculation time concerning the resolution of the DSM

The calculation time for each algorithm by resolution of the DSM was measured and visualized in Table 2 and Fig. 7. The time difference was marginal when calculated for a 100 × 100 DSM, but this significantly increases as the DSM resolution increases. The time difference for SBC and VBC(A) was over 20 h for a 900 × 900 DSM. These results show that the calculation time for SBC is the shortest which is similar to VBC(P). VBC(L) has the third shortest time, and VBC(A) requires the longest time.

The plots of calculation time and modified x values are shown in Fig. 8. The modified x values are $(n/100)^2$ for SBC, $(n/100)^3$ for VBC(L), $(n/100)^4$ for VBC(A), and $(n/100)^2 \log_2 (n/100)$ for VBC(P). n is divided by 100 to reduce the coefficient in the equation. All plots show a linear correlation with an R^2 value over 0.99. Therefore, all measured calculation times are in accordance with the theoretical

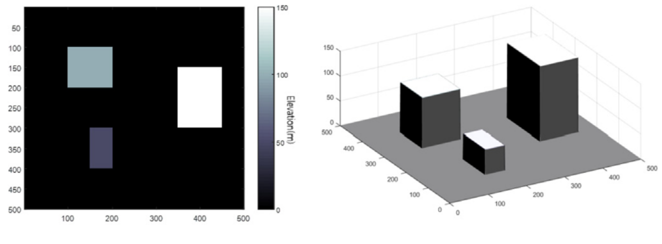

(a) Virtual DSM

(b) 3D view of virtual DSM

Fig. 6. (a) Orthogonal view of a virtual DSM and (b) 3D view of a virtual DSM.

Table 2
Measured calculation time concerning the resolution of the DSM.

resolution	Shadow	Line	All data	Pyramid
100 × 100	15.6	8.3	9.8	10.5
200 × 200	65.9	69.8	145.6	58.4
300 × 300	153.0	256.8	744.3	139.1
400 × 400	274.2	609.8	2534.7	271.2
500 × 500	412.7	1190.6	6433.9	449.3
600 × 600	598.2	2039.5	13,673.4	650.8
700 × 700	798.0	3241.8	26,937.8	991.6
800 × 800	1051.7	5167.0	46,023.7	1285.4
900 × 900	1331.4	6989.4	75,980.7	1693.1

time complexity. Also, all trend lines show a small y-intercept. This means other processes, apart from calculation shadowing, have little influence on the total calculation time.

4.2. Accuracy concerning the resolution of DSM

The measured rRMSE is shown in Fig. 9. All VBCs show a steady rRMSE when the resolution of the DSM is over 500 × 500. Only results with a resolution smaller than 300 × 300 show a high rRMSE. Although a high rRMSE is shown for lower resolutions, the absolute values are small as the maximum rRMSE is less than 0.05. The results for VBC(L) show the smallest error and have the most stable form. The results for VBC(A) show a slightly increase in error as the resolution increases, but the difference is marginal. The results for VBC(P) show the biggest decrease in error as the resolution increases, but it has a less error than VBC(A).

The measured rMBE is shown in Fig. 10. The trend of this graph is similar to the rRMSE graph. Absolute values of all rMBE are lower than 0.02. The VBC(L) shows the lowest error and the most consistent trend. VBC(A) shows a positive bias at first, but later becomes a negative bias as the resolution increases. The VBC(P) shows a continuously decreasing rMBE as the resolution of the DSM increases. It is positively biased; however, the absolute rMBE becomes smaller than VBC(A) when the resolution is over 400 × 400.

4.3. Time comparison concerning the sky division resolution

The calculation time for each algorithm is visualized in Fig. 11. The SBC shows an increase in calculation time when either the NZ or NA increases while the calculation time for the VBC is only affected by the NA. The VBC(P) is at its lowest when the NZ and NA is 60 and 180.

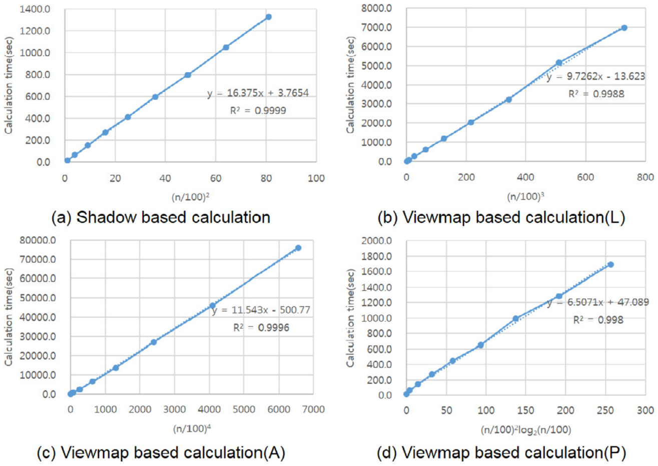

(a) Shadow based calculation

(b) Viewmap based calculation(L)

(c) Viewmap based calculation(A)

(d) Viewmap based calculation(P)

Fig. 8. Plots of calculation time with modified x values.

Like Section 4.1, a plot of the calculation time and modified x values is shown in Fig. 12. The modified x values are (z x a) for SBC, a for VBC(L) and VBC(A), and a^2 for VBC(P). All plots show a linear correlation and all R^2 values are over 0.99. Only VBC(L) shows a high y-intercept.

4.4. Accuracy concerning the sky division resolution

The measured rRMSE concerning different NZs and NAs is shown in Fig. 13. The rRMSE is more affected by the NA than the NZ. The SBC and VBC(L) show a high accuracy compared to the other algorithms. The VBC(A) and VBC(P) require a high NA to be accurate. In these algorithms, the rRMSE is over 0.1 when the NA is low.

The measured rMBE results are shown in Fig. 14. The SBC shows almost no biased results whereas all VBCs show a slightly negative bias when the NZ is low. The VBC(A) is negatively biased, and the VBC(P)s are positively biased when the NA is low. The bias for VBC(A) is over 0.06 when the NZ is 20 which is significant. The VBC(P) shows a bias of over 0.03 for the same NZ.

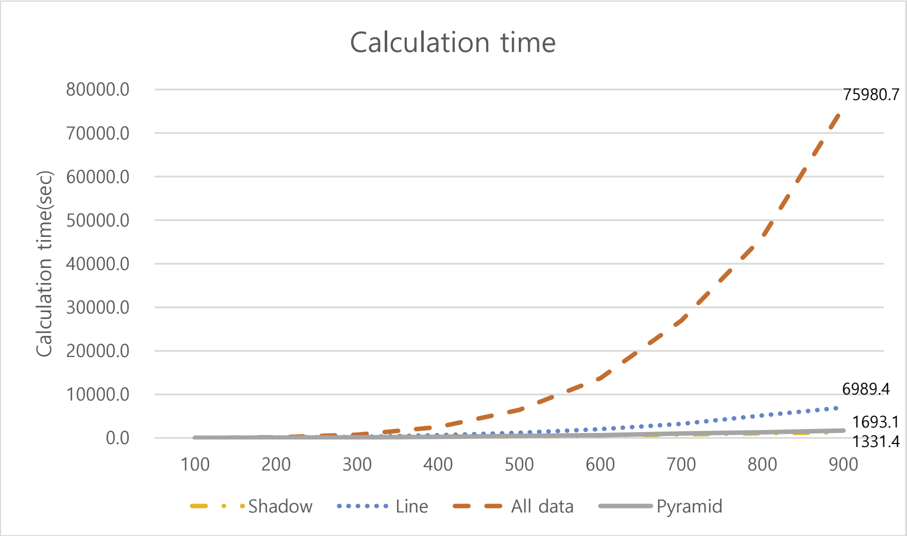

Fig. 7. Calculation time versus the resolution of the DSM.

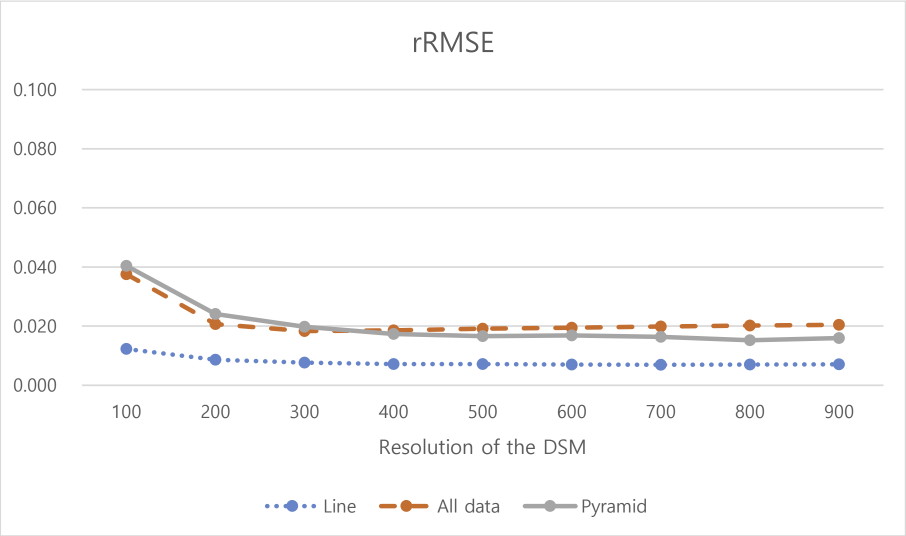

Fig. 9. Measured rRMSE concerning resolution of the DSM.

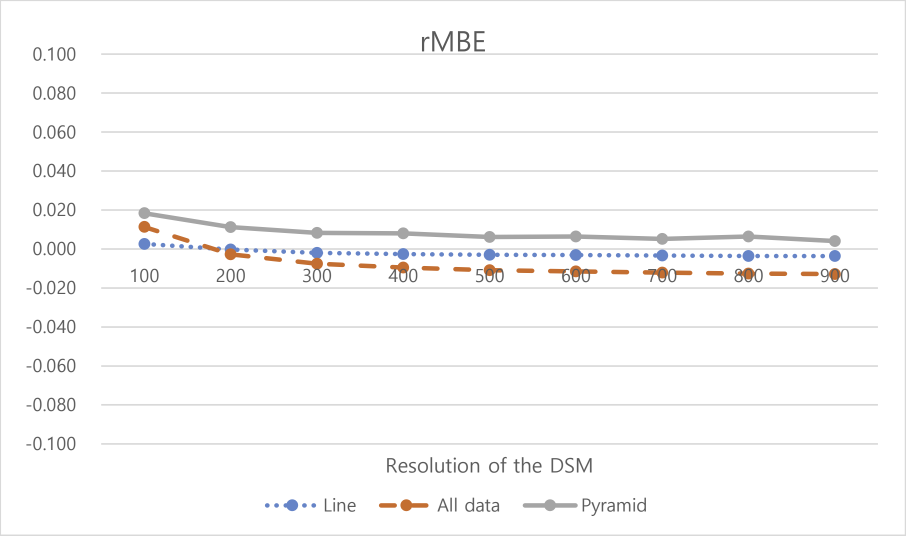

Fig. 10. Measured rMBE concerning the resolution of the DSM.

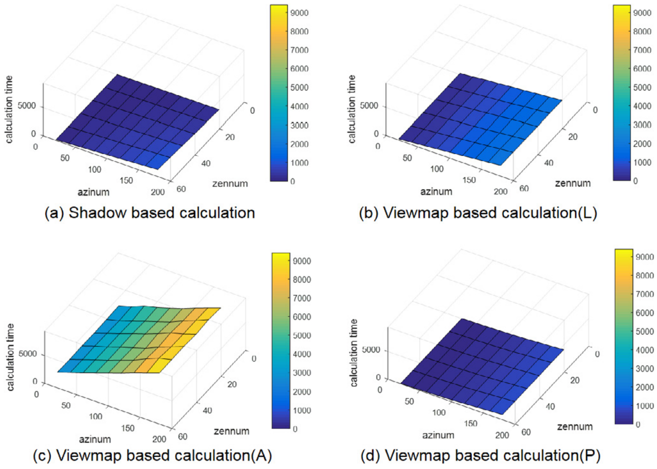

(a) Shadow based calculation

(b) Viewmap based calculation(L)

(c) Viewmap based calculation(A)

(d) Viewmap based calculation(P)

Fig. 11. Measured calculation time concerning the NZ and NA.

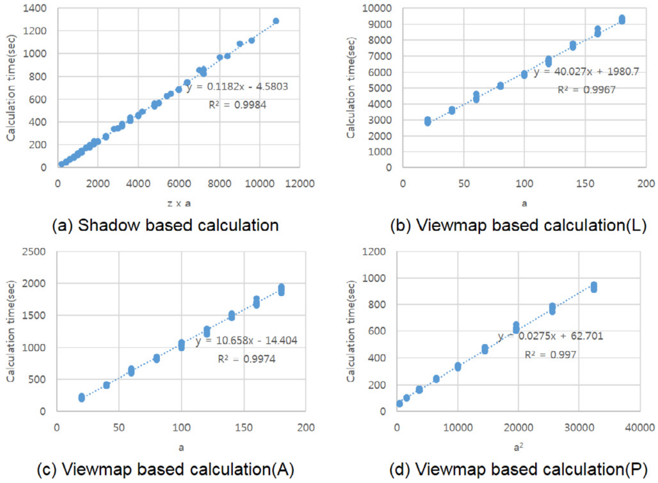

(a) Shadow based calculation

(b) Viewmap based calculation(L)

(c) Viewmap based calculation(A)

(d) Viewmap based calculation(P)

Fig. 12. Plot of calculation time with modified x values.

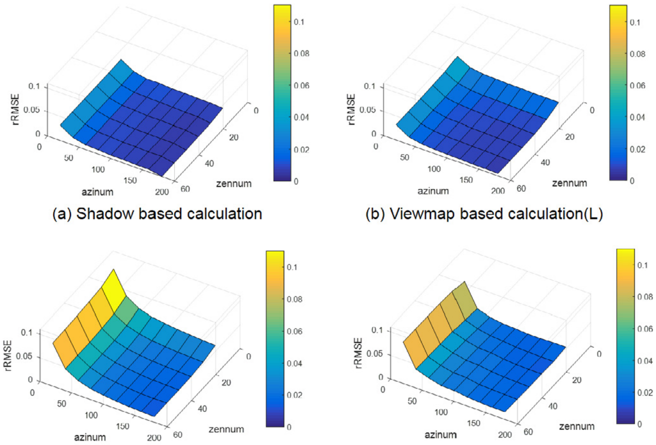

(a) Shadow based calculation (b) Viewmap based calculation(L)

(c) Viewmap based calculation(A) (d) Viewmap based calculation(P)

Fig. 13. Measured rRMSE with respect to the NZ and NA.

5. Discussion

5.1. Analysis of the calculation time

Trend lines for measured calculation times are in accordance with theoretical results. Both results regarding the resolution of the DSM and the resolution of sky division show strong correlations and high R^2. From these results, the calculation time was estimated from the equation of the plot of the calculation time and modified x values. The measured data show that a 900 × 900 DSM with 30 zenith and 120 azimuth values needs 22 min for SBC, 2 h for VBC(L), 21 h for VBC(A), and 28 min for VBC(P), respectively. Using these equations, a 20,000 × 20,000 DSM with the same sky division resolution is estimated to need 7.6 days, 2.5 years, 586 years, and 23 days, respectively to calculate each algorithm. As the calculation time increases, appropriate algorithms should be used to calculate data with high spatial resolutions.

Results for sky division resolution also show strong correlations. They show that the calculation time is proportional to the multiplication of these resolutions. SBC and VBC(P) are expected to be significantly affected because of their time complexity. However, the actual calculation time is significantly affected for VBC(L) and VBC(A) due to the fact that the total calculation time is much longer for these algorithms.

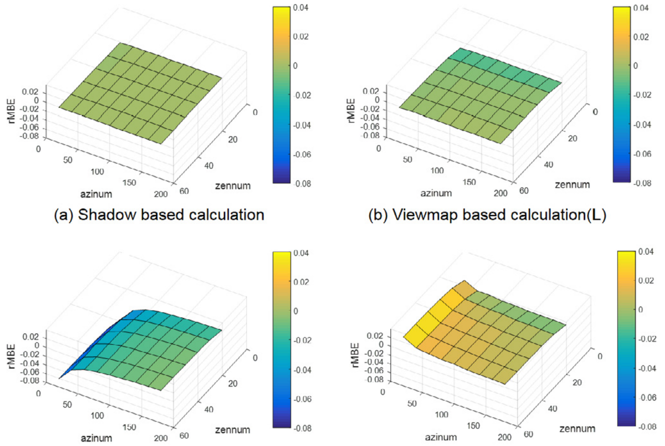

(a) Shadow based calculation (b) Viewmap based calculation(L)

(c) Viewmap based calculation(A) (d) Viewmap based calculation(P)

Fig. 14. Measured rMBE concerning the NZ and NA.

5.2. Analysis of accuracy

5.2.1. The effect of the resolution of the DSM

Results show that rRMSE is lower than 0.05 and rMBE is lower than 0.02, which can be evaluated as not significant. VBC(A) and VBC(P) show relatively low accuracy and little bias with low resolution DSMs. As shown in Fig. 15(a) and (b) and (c), the most significant error for a 100 × 100 resolution DSM occurs near the edge of the buildings' shadows. Although Fig. 15 shows the results of a pyramid dataset, other VBCs also show a similar distribution. These results are produced by a large NA. As there are few pixels near the view point but the NA is large, some azimuth angles have no pixels near the view point. These azimuth angles are determined as unshaded, but they are actually shadowed. This makes the edge of the shadow appear blurred and increases error and positive bias. This disappears when the resolution of the DSM increases as shown in Fig. 15(d) and (e) and (f).

Mostly, the rRMSE decreases as the resolution of the DSM increases, but only slightly increases for VBC(A). For the rMBE, this trend is similar; but for line scanning and VBC(A), this increases with an increased resolution. A slight increase in the bias for VBC(L) is created by scanning problems, which ignore data far from the view point. As the resolution of the DSM increases, the removed pixels also increases. Nevertheless, the total accuracy is higher than other VBCs. An increase in the rRMSE and rMBE for all-data scanning is explained by its exaggerated height problem. All-data scanning selects a maximum zenith angle for all pixels of the same azimuth, and this increases error for high-resolution DSMs. The VBC(P) does not have this problem. However, the results show that the average height causes an under estimation of the shadowing effect.

5.2.2. The effect of sky division resolution

The results for the rRMSE show a decreasing accuracy as the NZ and NA decrease. Exceptionally, VBC(P) shows a slight increase in rRMSE with an increase in the NZ. Detection of differences between the average height and original height may cause this trend, but the value is not significant. A NZ of 10–60 does not cause a significant difference. The results for VBC(L) for the two different NZ show almost the same results (Fig. 16). The area between the two buildings shows some differences, but this does not cause a significant error. The results of the other algorithms also show similar patterns. Nevertheless, the NA has a major influence on accuracy. The results of the SBC for the two different NA are shown in Fig. 17. When the NA is small, discontinuity of distribution becomes larger as shown in Fig. 17 (a).

All VBCs show a slight negative bias when the NZ is low, but this is not significant. VBC(A) shows a more negative bias when the NA is low, and VBC(P) shows the opposite result. The reason for this is similar to that for the accuracy analysis of the resolution of the DSM. VBC(A) sets a higher height as the number of pixels of the same azimuth increases. VBC(P) creates larger pixel sizes when the NA increases, which causes a lower height in the pyramid dataset. These differences produce different biases.

The values of the rRMSEs are lower than 0.05 when the NA is larger than 60. SBC and VBC(L) show a rRMSE below 0.04 when the NA is 20. These two algorithms show a high accuracy for both analyses. However, VBC(A), and VBC(P) show a relatively low accuracy of about 0.1 rRMSE when the NA is low. In other words, these two algorithms need to have an NA that is set at a sufficient high value.

5.3. Advantages of proposed new algorithm

In this study, SBC is evaluated as a method for simple results and VBC is evaluated as a method for detailed results. SBC can calculate

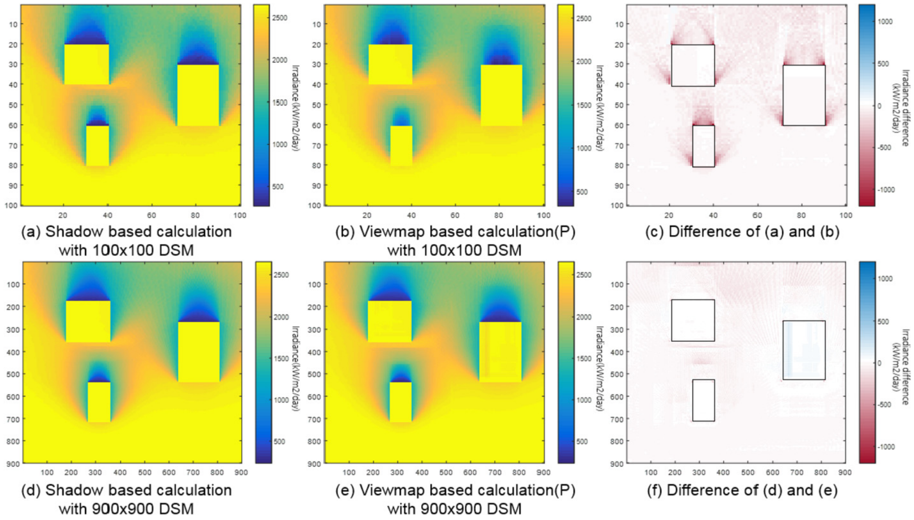

(a) Shadow based calculation with 100x100 DSM

(b) Viewmap based calculation(P) with 100x100 DSM

(c) Difference of (a) and (b)

(d) Shadow based calculation with 900x900 DSM

(e) Viewmap based calculation(P) with 900x900 DSM

(f) Difference of (d) and (e)

Fig. 15. Solar potential maps with a 100 × 100 resolution for the DSM made by (a) SBC, (b) VBC(P), (c) the difference of (a) and (b). A solar potential map with a 900 × 900 resolution for the DSM (d) SBC, (e) VBC(P) and (f) the difference of (d) and (e). Black lines show the shape of the DSM.

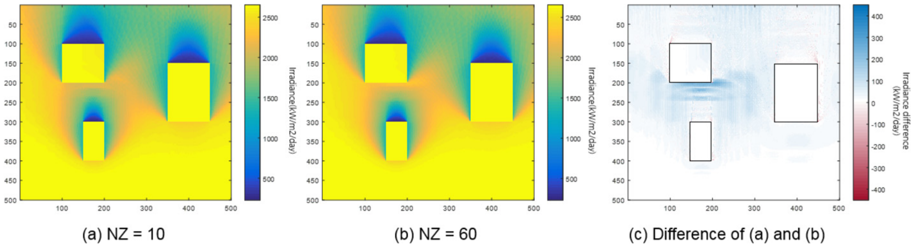

(a) NZ = 10

(b) NZ = 60

(c) Difference of (a) and (b)

Fig. 16. Solar potential maps created by (a) VBC(L) with NZ 60, (b) SBC with NZ 10, and (c) the difference of (a) and (b). Black lines show the shape of the DSM.

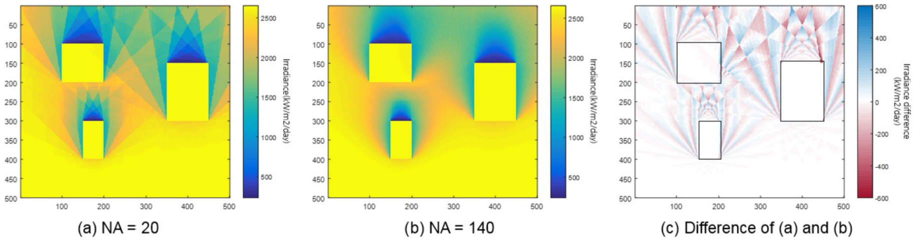

(a) NA = 20

(b) NA = 140

(c) Difference of (a) and (b)

Fig. 17. Solar potential maps created by SBC with NA (a) 20, (b) 140, and (c) the difference of (a) and (b). Black lines show the shape of the DSM.

simple solar potential maps rapidly. In contrast, VBC is slower than SBC but can calculate detailed results. For example, the VBC can apply the differences of the Sunmap in each position and can generate a potential map of different panel systems in each position. Also, Viewmap can be used in many analyses such as the effect of nearby objects, optimization of solar panel angles, and summation of different scale surface maps. In addition, it can easily calculate the portion of specific areas and generate multiple periods or hourly results at once. SBC is suitable to calculate only one result map per one process. Nevertheless, VBC is not appropriate for high-resolution DSMs because existing algorithms for calculating Viewmaps need high computational power.

This study proposed a new algorithm using a pyramid dataset. Table 3 summarizes the features and results for each algorithm. The new VBC(P) can calculate Viewmaps rapidly, which means it can utilize features of VBC and calculate detailed results rapidly. Although this algorithm requires a higher sky division resolution to be accurate, the calculation time is faster than existing VBCs. As time complexity ratio compared to VBC(L) is log(n)/n, the new algorithm can be faster than previous VBCs more than 100 times when spatial resolution is over 10,000. If target accuracy is below 0.02 of rRMSE, VBC(P) should have 3 times higher AN than VBC(L). In this case, VBC(P) can be 30 times faster than VBC(L) with similar accuracy. It is slightly slower than SBC; however, the new algorithm has the advantages of VBC and is faster when the study area is a portion of the total area or when the moving window method is used. Accuracy and bias are not significant if a high sky division resolution is used. Therefore, this new algorithm makes it possible to rapidly analyze and calculate detailed solar potential in high resolution data.

5.4. Limitations

There are some limitations present in this study. First, all calculations are operated in Matlab, which has distinctive performance characteristics and does not represent all programming languages. The calculation time can be different for each language. Nonetheless, as the results are in accordance with theoretical time

Table 3
Comparison of algorithms for the calculation of shadowing.

Algorithm for shadowing	Viewmap	Time complexity	Calculation time (criteria)	Recommended resolution of sky division (AN for rRMSE<0.02)	Bias (criteria)
Shadow Based Calculation	Not generated	O $(nmza)$	Fast (<O (n^3))	Low (AN>30)	Marginal (<0.01)
Viewmap Based Calculation(L)	Generated	O $(nma(n + m))$	Moderate (<O (n^4))	Low (AN>30)	Marginal (<0.01)
Viewmap Based Calculation(A)	Generated	O $(n^2\mathrm{m}^2a)$	Slow (>O (n^4))	High (AN>100)	Negative with small NA
Viewmap Based Calculation(P)	Generated	O $(nma^2\log(n))$	Fast (<O (n^3))	High (AN>100)	Positive with small NA

complexities, the trends will not change significantly for other programming languages.

Second, the algorithms in this study do not consider reflection and transmission. There is significant reflected irradiance from surrounding objects; however, this study only considers beam and diffuse irradiance from sky hemisphere. Transmission can make a difference as some structures are transparent and natural objects like trees transmit irradiance. The irradiance physical model containing the sky diffuse model can also be changed. Further studies may consider these factors.

Third, this study uses only DSM or DEM type 2.5D data which cannot describe complex geometries in urban areas. There are several structures that have empty spaces or complex shapes. These structures are represented as simple solid geometry in 2.5D data, which presents results different to the actual environment. To consider 3D data, new types of data should be considered and longer calculation times will be required.

6. Conclusion

Resolutions for DSMs are increasing because of new technologies. To analyze high-resolution data, appropriate algorithms should be selected. The first objective of this study was to propose a new rapid and accurate algorithm. This algorithm uses a pyramid dataset to demonstrate effective performance. It calculates Viewmaps with high-resolution DSMs quickly. In specific studies, it was shown that the calculation time can be faster than SBC. Some problems related to the accuracy of results were encountered, but these are not significant if high-resolutions of sky division is used. Therefore, the proposed new algorithm demonstrates high potential for the calculation of solar potential.

The second objective was to compare the different algorithms available for calculating shadowing. Four different algorithms were compared and each algorithm showed different features. Although the proposed algorithm demonstrates high potential, it does not mean that this algorithm gives optimal answers. SBC has strengths in efficiency, and line scanning algorithms can calculate transmission easily. The selection of resolution is also an important factor. As an excessive increase in resolutions can result in low efficiency, the optimization of variables should be considered. The results of this study will aid in selecting proper algorithms and resolutions, and this optimization will reduce inefficiencies and produce more reliable results.

Acknowledgement

This work was supported by the National Research Foundation of Korea (NRF) and funded by the Korean government (MSIT; Ministry of Science and ICT) (No. NRF-2017R1A2B4007623).

References

[1] S. Freitas, C. Catita, P. Redweik, M.C. Brito, Modelling solar potential in the urban environment: state-of-the-art review, Renew. Sustain. Energy Rev. 41 (2015) 915–931.

[2] W. GJ, The RADIANCE lighting simulation and rendering system, in: Proceedings of the 21st Annual Conference on Computer Graphics and Interactive Techniques, SIGGRAPH '94, 1994, pp. 459–472.

[3] R. Compagnon, Solar and daylight availability in the urban fabric, Energy Build. 36 (4) (2004) 321–328.

[4] D. Robinson, Urban morphology and indicators of radiation availability, Sol. Energy 80 (12) (2006) 1643–1648.

[5] M. Suri, J. Hofierka, The solar radiation model for Open source GIS: implementation and applications, in: Open Source GIS – GRASS Users Conference, 2002, pp. 11–13.

[6] J. Hofierka, J. Kanuk, Assessment of photovoltaic potential in urban areas using open-source solar radiation tools, Renew. Energy 34 (10) (2009) 2206–2214.

[7] P. Rich, P. Fu, Design and implementation of the Solar Analyst: an ArcView extension for modeling solar radiation at landscape scales, in: Proceedings of the 19th Annual ESRI User Conference, 1999.

[8] L.K. Wiginton, H.T. Nguyen, J.M. Pearce, Quantifying rooftop solar photovoltaic potential for regional renewable energy policy, Comput Environ Urban 34 (4) (2010) 345–357.

[9] M.C. Brito, N. Gomes, T. Santos, J.A. Tenedorio, Photovoltaic potential in a Lisbon suburb using LiDAR data, Sol. Energy 86 (1) (2012) 283–288.

[10] T. Santos, N. Gomes, S. Freire, M.C. Brito, L. Santos, J.A. Tenedorio, Applications of solar mapping in the urban environment, Appl. Geogr. 51 (2014) 48–57.

[11] J.J. Sarralde, D.J. Quinn, D. Wiesniann, K. Steemers, Solar energy and urban morphology: scenarios for increasing the renewable energy potential of neighbourhoods in London, Renew. Energy 73 (2015) 10–17.

[12] K. Suomalainen, V. Wang, B. Sharp, Rooftop solar potential based on LiDAR data: bottom-up assessment at neighbourhood level, Renew. Energy 111 (2017) 463–475.

[13] C. Chatzipoulka, R. Compagnon, M. Nikolopoulou, Urban geometry and solar availability on fa ades and ground of real urban forms: using London as a case study, Sol. Energy 138 (2016) 53–66.

[14] J. Mardaljevic, Simulation of annual daylighting profiles for internal illuminance, Light. Res. Technol. 32 (3) (2000) 111–118.

[15] J.A. Jakubiec, C.F. Reinhart, A method for predicting city-wide electricity gains from photovoltaic panels based on LiDAR and GIS data combined with hourly Daysim simulations, Sol. Energy 93 (2013) 127–143.

[16] R. Erdelyi, Y.M. Wang, W.S. Guo, E. Hanna, G. Colantuono, Three-dimensional SOlar RAdiation Model (SORAM) and its application to 3-D urban planning, Sol. Energy 101 (2014) 63–73.

[17] J. Hofierka, M. Zlocha, A new 3-D solar radiation model for 3-D city models, T Gis 16 (5) (2012) 681–690.

[18] P. Redweik, C. Catita, M. Brito, Solar energy potential on roofs and facades in an urban landscape, Sol. Energy 97 (2013) 332–341.

[19] C. Catita, P. Redweik, J. Pereira, M.C. Brito, Extending solar potential analysis in buildings to vertical facades, Comput Geosci-Uk 66 (2014) 1–12.

[20] M.C. Brito, S. Freitas, S. Guimaraes, C. Catita, P. Redweik, The importance of facades for the solar PV potential of a Mediterranean city using LiDAR data, Renew. Energy 111 (2017) 85–94.

[21] J. Teller, S. Azar, TOWNSCOPE II - a computer system to support solar access decision-making, Sol. Energy 70 (3) (2001) 187–200.

[22] L.R. Rodriguez, E. Duminil, J.S. Ramos, U. Eicker, Assessment of the photovoltaic potential at urban level based on 3D city models: a case study and new methodological approach, Sol. Energy 146 (2017) 264–275.

[23] J.A. Ruiz-Arias, J. Tovar-Pescador, D. Pozo-Vázquez, H. Alsamamra, A comparative analysis of DEM-based models to estimate the solar radiation in mountainous terrain, Int. J. Geogr. Inf. Sci. 23 (8) (2009) 1049–1076.

[24] M. AJ, Sky Subdivision, Natural Frequency, 2011.

[25] R. Dubayah, P.M. Rich, Topographic solar-radiation models for Gis, Int. J. Geogr. Inf. Syst. 9 (4) (1995) 405–419.